



Tuning composition in graded AlGa_N channel HEMTs toward improved linearity for low-noise radio-frequency amplifiers

Downloaded from: <https://research.chalmers.se>, 2025-12-04 23:39 UTC

Citation for the original published paper (version of record):

Papamichail, A., Persson, A., Richter, S. et al (2023). Tuning composition in graded AlGa_N channel HEMTs toward improved linearity for low-noise radio-frequency amplifiers. *Applied Physics Letters*, 122(15). <http://dx.doi.org/10.1063/5.0141517>

N.B. When citing this work, cite the original published paper.

RESEARCH ARTICLE | APRIL 10 2023

Tuning composition in graded AlGa_N channel HEMTs toward improved linearity for low-noise radio-frequency amplifiers



A. Papamichail ; A. R. Persson; S. Richter; ... et. al



Check for updates

Appl. Phys. Lett. 122, 153501 (2023)<https://doi.org/10.1063/5.0141517>View
OnlineExport
Citation

CrossMark

Articles You May Be Interested In

Optimization of linearity at high electrical field for dual threshold coupling AlGa_N/Ga_N HEMT applied in Ka-band applications

Appl. Phys. Lett. (August 2022)

Fabrication and comparative study of DC and low frequency noise characterization of Ga_N/AlGa_N based MOS-HEMT and HEMT

Journal of Vacuum Science & Technology B (August 2017)

Temperature-dependent characteristics for the p-type CuO gate HEMT and high-k HfO₂ MIS-HEMT on the Si substrates

AIP Advances (October 2021)



A total solution for low-temperature characterization

[Learn more >](#)



Tuning composition in graded AlGaIn channel HEMTs toward improved linearity for low-noise radio-frequency amplifiers

Cite as: Appl. Phys. Lett. **122**, 153501 (2023); doi: [10.1063/5.0141517](https://doi.org/10.1063/5.0141517)

Submitted: 6 January 2023 · Accepted: 24 March 2023 ·

Published Online: 10 April 2023















View Online



Export Citation



CrossMark

A. Papamichail,^{1,a)}  A. R. Persson,^{1,2}  S. Richter,^{1,3,4}  P. Kühne,^{1,3}  V. Stanishev,^{1,3}  P. O. Å. Persson,² 
R. Ferrand-Drake Del Castillo,⁵  M. Thorsell,^{5,6}  H. Hjelmgren,⁵  P. P. Paskov,¹  N. Rorsman,⁵ 
and V. Darakchieva^{1,3,4,a)} 

AFFILIATIONS

¹Center for III-Nitride Technology, C3NiT-Janzén, Department of Physics, Chemistry and Biology (IFM), Linköping University, SE-58183 Linköping, Sweden

²Thin Film Physics, Department of Physics, Chemistry and Biology (IFM), Linköping University, Linköping SE-58183, Sweden

³Terahertz Materials Analysis Center, THeMAC, Linköping University, SE-58183 Linköping, Sweden

⁴Solid State Physics and NanoLund, Lund University, 221 00 Lund, Sweden

⁵Department of Microtechnology and Nanoscience, Chalmers University of Technology, SE-41296 Göteborg, Sweden

⁶Saab AB, SE-11122 Stockholm, Sweden

^{a)}Authors to whom correspondence should be addressed: alexis.papamichail@liu.se and vanya.darakchieva@liu.se

ABSTRACT

Compositionally graded channel AlGaIn/GaN high electron mobility transistors (HEMTs) offer a promising route to improve device linearity, which is necessary for low-noise radio-frequency amplifiers. In this work, we demonstrate different grading profiles of a 10-nm-thick $\text{Al}_x\text{Ga}_{1-x}\text{N}$ channel from $x=0$ to $x=0.1$ using hot-wall metal-organic chemical vapor deposition (MOCVD). The growth process is developed by optimizing the channel grading and the channel-to-barrier transition. For this purpose, the Al-profiles and the interface sharpness, as determined from scanning transmission electron microscopy combined with energy-dispersive x-ray spectroscopy, are correlated with specific MOCVD process parameters. The results are linked to the channel properties (electron density, electron mobility, and sheet resistance) obtained by contactless Hall and terahertz optical Hall effect measurements coupled with simulations from solving self-consistently Poisson and Schrödinger equations. The impact of incorporating a thin AlN interlayer between the graded channel and the barrier layer on the HEMT properties is investigated and discussed. The optimized graded channel HEMT structure is found to have similarly high electron density ($\sim 9 \times 10^{12} \text{ cm}^{-2}$) as the non-graded conventional structure, though the mobility drops from $\sim 2360 \text{ cm}^2/\text{Vs}$ in the conventional to $\sim 960 \text{ cm}^2/\text{Vs}$ in the graded structure. The transconductance g_m of the linearly graded channel HEMTs is shown to be flatter with smaller g'_m and g''_m as compared to the conventional non-graded channel HEMT implying improved device linearity.

© 2023 Author(s). All article content, except where otherwise noted, is licensed under a Creative Commons Attribution (CC BY) license (<http://creativecommons.org/licenses/by/4.0/>). <https://doi.org/10.1063/5.0141517>

Today's rapid development of radio-frequency (RF) communication technology requires utilization of optimized devices to meet the demands of high-frequency power amplifiers.¹ AlGaIn/GaN high electron mobility transistors (HEMTs) have been widely explored for RF technology applications, delivering high power and high gain. However, a weak point of such devices is their inherent non-linear behavior at high power input signal, which results in gain compression and signal distortion.² Modifying the two-dimensional electron gas (2DEG) confinement alters the 2DEG distribution and results in formation of a

three-dimensional electron gas (3DEG) in the HEMT channel.³ This modification is predicted to improve the small-signal linearity rendering devices with characteristics relevant for use in low-noise amplifiers (LNAs) as well as providing improved large-signal linearity. Indeed, a spatially broader electron distribution improves the HEMT linearity,^{2,4–8} rendering a constant cutoff frequency f_T and maximum oscillation frequency f_{max} over a wider range of input power. 3DEGs in AlGaIn/GaN heterostructures can be formed through polarization doping by compositionally grading with Al the GaN HEMT channel.⁹

Although graded channel HEMTs are emerging as very promising devices for linear RF LNAs,^{10–13} the understanding of the channel grading effects on the 3DEG properties is still limited. For example, there is no information regarding the actual Al grading profiles and their interrelation with charge carrier properties. Moreover, from a practical point of view, the development of the growth process for graded channel HEMTs is not trivial. Precise control of the compositional grading (variation of the Al-content) and the thickness (in the range of 10 nm or less) of the graded channel layer are required in order to achieve a 3DEG appropriate for improved device linearity. Additionally, achieving sharp interfaces between adjacent layers in the HEMT structure is critical for the transport properties and device performance. The aforementioned practical difficulties render the metal-organic chemical vapor deposition (MOCVD) of graded channel HEMT structures experimentally challenging. Thus, a comprehensive study combining insights on the material growth with device simulations and realization is required for getting a better understanding of the graded channel HEMT performance and structure optimization.

In this work, we present various approaches to realize graded channel AlGa_xGaN/GaN HEMT structures grown by MOCVD. We develop the growth process of a graded channel with an Al-content from 0% to 10% with three different grading profiles: (i) exponential grading, (ii) hybrid hyperbolic tangent—linear grading, and (iii) linear grading, combined with further tuning of the channel-to-barrier transition. The effect of introducing a thin AlN interlayer between the graded channel and the barrier layers on the HEMT transport properties is also investigated. The experimentally measured 2DEG/3DEG properties are discussed in comparison with simulations of the carrier density distribution related to the type of grading and the interface structure. Finally, two HEMT devices—an optimized linearly graded channel HEMT and a conventional non-graded AlGa_xGaN/GaN HEMT—are fabricated and compared in terms of device performance.

Graded channel and conventional AlGa_xGaN HEMT structures (schematics shown in Fig. 1) were grown in a horizontal hot-wall MOCVD reactor (VP508GFR, Aixtron) on semi-insulating 4H-SiC substrates with (0001) orientation. The growth process was performed under a 2 l/min constant ammonia (NH₃) flow and a mixture of N₂ and H₂ as carrier gases. NH₃, trimethylaluminum (TMAl), and trimethylgallium (TMGa) were used as the N, Al, and Ga precursors, respectively. Prior to the growth, the SiC substrates were etched under high-

temperature, 1340 °C, and H₂-rich environment for step-like surface preparation. Thereafter, a 60 nm thick AlN nucleation layer was grown at 1250 °C with a V/III ratio of 1260. All the layers above the AlN nucleation layer were grown at a temperature of 1070 °C and a constant pressure of 100 mbar. The subsequent 1.1 μm thick unintentionally doped (UID) GaN buffer layer was followed by a graded channel layer in the case of samples S₁–S₅, while samples S₆–S₈ have conventional non-graded GaN channels. The barrier layer of all samples (S₁–S₈) consisted of a (11–15)-nm-thick Al_{0.30}Ga_{0.70}N layer. The growth was finished with a 2–3 nm GaN cap layer for samples S₃–S₈. An AlN interlayer was added between the channel and the barrier layer in the case of samples S₄, S₅, S₇, and S₈. During the AlN interlayer growth, the Al precursor (TMAl) flow was maintained for 15 s (S₄ and S₇) and 30 s (S₅ and S₈).

Three different approaches were implemented for the growth of the graded channel layer in samples S₁–S₃ in order to achieve distinctively different types of grading. The TMGa precursor flow was kept constant while the TMAl flow was varied: (i) TMGa flow was at 2.2 ml/min, and TMAl flow varied from 0 to 0.23 ml/min over 33 s (sample S₁), (ii) TMGa flow was at 1.4 ml/min, and TMAl flow varied from 0.05 to 0.19 ml/min over 105 s (sample S₂), and (iii) TMGa flow was at 1.4 ml/min, and TMAl flow varied from 0.02 to 0.13 ml/min over 110 s (sample S₃).

The surface root mean square (RMS) roughness of the structures was lower than 0.45 nm over a $5 \times 5 \mu\text{m}^2$ area according to the atomic force microscopy (AFM) measurements on samples S₁–S₃ (see [supplementary material](#) Fig. S1). The low surface roughness is indicative of the smoothness of the channel/barrier interface where the 2DEG/3DEG is formed. In order to determine the thicknesses of the AlN nucleation layer, the GaN buffer layer, and the Al_xGa_{1-x}N barrier layer, variable angle spectroscopic ellipsometry (VASE) data were measured and fit to an appropriate optical model. The VASE measurements were performed on a J. A. Woollam RC2-XI ellipsometer in the near-infrared to ultraviolet spectral range (0.7–5.9 eV). Note that the thickness and composition of the graded Al_xGa_{1-x}N layer are taken from the scanning transmission electron microscopy (STEM) and energy-dispersive x-ray spectroscopy (EDS) measurements as input for the VASE data analysis (see the supplementary for further details). Reciprocal space maps (RSMs) around the GaN asymmetric 10 $\bar{1}$ 5 reciprocal lattice points were recorded using a PANalytical Empyrean X-ray diffractometer in 2-axis configuration with a hybrid monochromator at the incident X-ray beam and the detector in the scanning line mode (see [supplementary material](#) Fig. S3). The Al-content in the Al_xGa_{1-x}N barrier layers was determined from the *a* and *c* lattice parameters obtained from the RSMs assuming validity of Vegard's law¹⁴ and using the strain-free lattice parameters of GaN and AlN.^{15,16} The RSM measurements also revealed that the AlGa_x epilayers were pseudomorphically grown to the thick GaN buffer layer for all Al compositions. The density of screw and edge type dislocations in the GaN buffer layers was evaluated from the respective tilt and twist angles using the lattice parameters from Ref. 15 and following the methods described by Metzger *et al.*¹⁷ and Srikant *et al.*¹⁸ The dislocation densities in the very thin (up to 10 nm) graded layers are considered similar to those in the thick GaN buffer layer and are found to be $2.5 \times 10^7 \text{ cm}^{-2}$ for screw and $4.7 \times 10^8 \text{ cm}^{-2}$ for edge type dislocations.

The 2DEG/3DEG mobility μ and sheet density N_s were obtained at room temperature by a contactless microwave (10 GHz) based

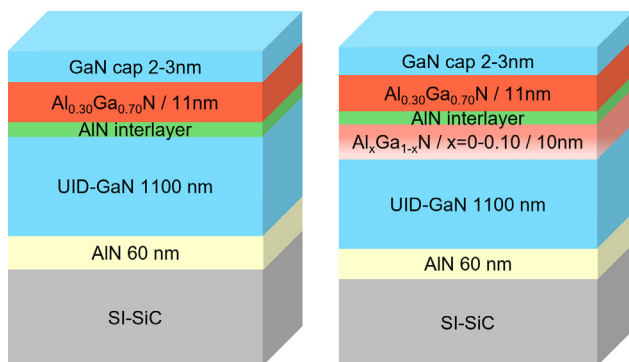


FIG. 1. Conventional non-graded channel HEMT structure (left) and graded channel HEMT structure (right).

TABLE I. Summary of the structural details and the 2DEG/3DEG properties of the studied HEMT structures.

Sample	S ₁	S ₂	S ₃	S ₄	S ₅	S ₆	S ₇	S ₈
Channel grading	Exponential	Linear-tanh	Linear	Linear	Linear	None	None	None
Channel-barrier transition	Smooth	Smooth	Smooth	Sharp	Sharp	Smooth	Sharp	Sharp
AlN interlayer	No	No	No	0.5 nm	1.5 nm	No	0.5 nm	1.5 nm
N_s ($\times 10^{12} \text{ cm}^{-2}$)	10.50 ± 1.81^a	8.11 ± 0.64^a	9.04 ± 0.04^b	8.51 ± 0.09^b	9.95 ± 0.07^b	7.24 ± 0.01^b	8.90 ± 0.04^b	9.06 ± 0.01^b
μ (cm^2/Vs)	964 ± 62^a	907 ± 64^a	943 ± 8^b	904 ± 15^b	958 ± 12^b	1864 ± 37^b	2087 ± 17^b	2368 ± 24^b
R_s (Ω/sq)	617	731	723	792	686	463	338	290

^aTHz-OHE.^bContactless Hall (Leighton).

method referred to as contactless Hall (Leighton LEI1600). For samples S₁ and S₂, the 2DEG properties and the sheet resistance were determined by cavity-enhanced terahertz optical Hall effect (THz-OHE) measurements due to sample size limitations of the Leighton instrument. The THz-OHE measurements were performed at room temperature and magnetic field of $\pm 0.6 \text{ T}$,^{19,20} and the experimental results were analyzed using the approaches described in Refs. 19 and 21. The THz-OHE and contactless Hall techniques were shown to deliver consistent values of the 2DEG properties for samples with relatively high sheet resistance, such as for samples S₁–S₂. In our case, this allows for meaningful comparisons between the samples that were measured by the two different techniques. The sheet resistance of the samples was measured by a contactless Eddy current-based method using an Eichhorn Hausmann MX604 tool with a working range of 50–3000 Ω/sq . The Al compositional profiles and quality of the interfaces were studied by STEM combined with EDS. Analysis was performed using the double corrected Linköping FEI Titan³ 60–300 microscope, operated at 300 kV. The built-in Super-X/Quantax EDS system (Bruker) was employed, and the absolute quantifications were made using the Esprit software and its built-in calibrations for TEM-EDS. The $\sim 30\%$ Al measured in the barrier, by EDS, is benchmarked to the corresponding Al-content extracted from RSM, which is also $\sim 30\%$ Al. Hence, it acts as its own reference, and the absolute values obtained from EDS are deemed reliable. Four EDS maps from four different sites per sample were acquired and integrated along the interface and subsequently quantified. The profiles were finally averaged for each sample for more reliable data. The structural and 2DEG/3DEG properties of all samples are summarized in Table I.

Band bendings and charge density distribution in the HEMT structures were obtained from solving self-consistently Poisson and Schrödinger equations, utilizing the numerical solver by Snider.^{22,23} The Al-profiles from the EDS measurements were used for the simulations, where a piece-wise linear approximation was adopted for samples S₁ and S₂, and single linear grading in agreement with the experimentally observed trends was employed for samples S₃–S₅. The AlN interlayers were also taken into account in the simulations accordingly, while the SiC substrate and the AlN nucleation layer were not considered.

Figure 2 shows the Al-profiles obtained from the EDS measurements across the graded channel and barrier layers for samples S₁, S₂, and S₃. If the grading in the channel starts directly from $x=0$ and with the TMGa flow used for the GaN growth (S₁), the Al-content increases very slowly to $\sim 2\%$ in the relatively fast growth process (33s)

before reaching the intended $x=0.1$. This results in an exponential channel grading for S₁. The HEMT structure can also be viewed as consisting of a $\sim 10\text{-nm}$ -thick AlGaIn channel with 1%–2% of Al and a diffuse interface to the barrier layer. On the other hand, if the grading starts from a non-zero value, i.e., with a TMAI/TMGa ratio of 3.6% and a TMGa flow value employed for the growth of the barrier layer (sample S₂), there is fast on-set of the Al grading, and the Al-content increases up to 15% across the channel thickness (Fig. 2). In this case, the S₂ channel has a hybrid linear-tanh grading profile. Finally, keeping the same TMGa but reducing the initial and final TMAI/TMGa ratios to 1.4% and 9.4%, respectively, results in a linearly graded Al_xGa_{1-x}N channel from $x=0$ to $x=0.1$ for S₃.

The 2DEG/3DEG density, N_s , in the samples with the different types of channel grading (S₁–S₃) is found to be similar, in the range of $(8 - 10.5) \times 10^{12} \text{ cm}^{-2}$ (Table I). This can be expected since the graded channel layers have similar thickness and similar Al-content in barrier layers. The mobility parameters were found to be $964 \text{ cm}^2/\text{Vs}$ for S₁, $907 \text{ cm}^2/\text{Vs}$ for S₂, and $943 \text{ cm}^2/\text{Vs}$ for S₃, which are significantly lower as compared to the typical mobility values in conventional non-graded HEMTs (see S₆ Table I and, e.g., Ref. 24). The latter is a result of the quasi-3D nature of the electrons and the enhanced

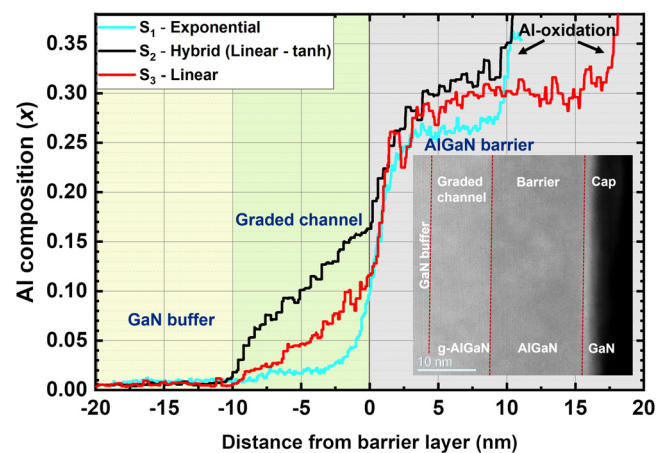


FIG. 2. Al-content profiles across the graded channel and barrier layers obtained from EDS: cyan—S₁ (exponential), black—S₂ (hybrid linear-tanh), and red—S₃ (linear). The inset shows a STEM image of the linearly graded channel HEMT structure S₃.

alloy scattering²⁵ in the graded channel. In addition, the channels in S_1 – S_3 are directly interfacing the barrier layers, which may result in a certain penetration of the 2DEG/3DEG electron wavefunction into the barrier layer, further enhancing the already present alloy scattering. The slightly higher 2DEG mobility for the exponentially graded channel structure (S_1) may be attributed to lesser alloy scattering within the AlGaIn channel having low Al-content for a larger proportion of its thickness as compared to samples S_2 and S_3 . Note that for S_1 , the definition of the channel thickness is to some extent arbitrary. However, the larger error bars of the mobility parameters for samples S_1 and S_2 prevent a more solid conclusion.

The simulated electron density distribution for the graded channels using the measured Al-profiles and thicknesses is compared with the respective profile for the non-graded channel HEMT structure with no AlN interlayer, sample S_6 , in Fig. 3(a). The carrier distribution in the exponentially graded channel (S_1) has an extended tail, but it is overall similar to that of the conventional non-graded channel sample

(S_6). Hence, no big influence on the transconductance flatness may be expected for a device based on this sample. The carrier distribution in the sample with hybrid profile (S_2) resembles that of the linearly graded sample (S_3) with a clear 3D nature of the electron gas spanning over 15–20 nm. A comparison between the 3DEG properties of these two samples (S_2 and S_3) shows that the linearly graded channel HEMT structure (S_3) has a higher mobility compared to the hybrid graded sample (S_2) (Table I).

In addition, S_3 has a sharper channel-barrier interface compared to sample S_2 (see Fig. 2), which is expected to result in a lesser penetration of the 3DEG in the barrier layer and, consequently, in a reduced alloy scattering. The slightly higher 3DEG density of S_3 is probably related to the slightly thicker barrier layer. Therefore, the linear channel grading profile (sample S_3) was selected for further optimization.

A widely employed method for improving the 2DEG mobility in conventional non-graded channel HEMTs is the introduction of a very thin AlN interlayer between the channel and the barrier layer, which reduces the alloy scattering in the barrier layer. Such a thin AlN layer acts as sharpening of the channel-barrier interface and, at the same time, provides an effective energy barrier confining the electrons in the channel region. Due to the large bandgap of AlN, the conduction band discontinuity at the interface is increased, and the electron wavefunction is better confined in the channel layer. Moreover, it was shown that the incorporation of an AlN interlayer is beneficial for short recovery time during operation of HEMTs used in RF LNAs because it prevents hot electrons from being captured in the bulk AlGaIn or at surface traps.²⁶ Indeed, for our conventional (non-graded) HEMT structures with AlN interlayers of 0.5 nm (S_7) and 1.5 nm (S_8), the mobility parameters increase noticeably as compared to the structure without an interlayer (S_6) (Fig. 4 and Table I). It is seen that the mobility can be improved more than 25% from ~ 1860 to ~ 2370 cm²/V s with increasing the AlN interlayer thickness from 0 to 1.5 nm. These results are in agreement with previous reports.^{24,27}

However, there are no studies in the literature considering the combination of an AlN interlayer with graded channel in HEMT structures. In order to investigate the effect of AlN interlayer incorporation on the 2DEG properties of a graded channel HEMT structure, two samples with AlN interlayers with thicknesses of 0.5 nm (S_4) and 1.5 nm (S_5) were fabricated adopting the growth conditions for the 10 nm thick linearly graded channel sample (S_3). In fact, the two AlN thicknesses may be considered as a smoother (0.5 nm for S_4) or sharper (1.5 nm for S_5) onset of the Al-content and of the transition to the Al_{0.30}Ga_{0.70}N barrier layer, respectively. The simulated electron density profiles and the 2DEG/3DEG properties of the graded channel HEMT structures with different thicknesses of the AlN interlayer are presented in Figs. 3(b) and 5, respectively, together with the corresponding results for S_8 . It is seen from Fig. 3(b) that a larger electron density is expected in the graded channel layer when a 1.5 nm AlN interlayer is added prior to the Al_{0.30}Ga_{0.70}N barrier. This is also reflected in the measured N_s data for sample S_5 (see Table I). In addition, from the simulations in Fig. 3(b), it is expected that the sample with the thicker AlN interlayer will show improved 2DEG transport properties since the largest portion of carriers is confined close to the channel-barrier interface. Consequently, an abrupt interface would reduce the alloy disorder scattering in the high Al-content AlGaIn barrier. However, the mobility in the linear profile HEMT structure with the 1.5 nm thick AlN interlayer (S_5) is very similar to the mobility of

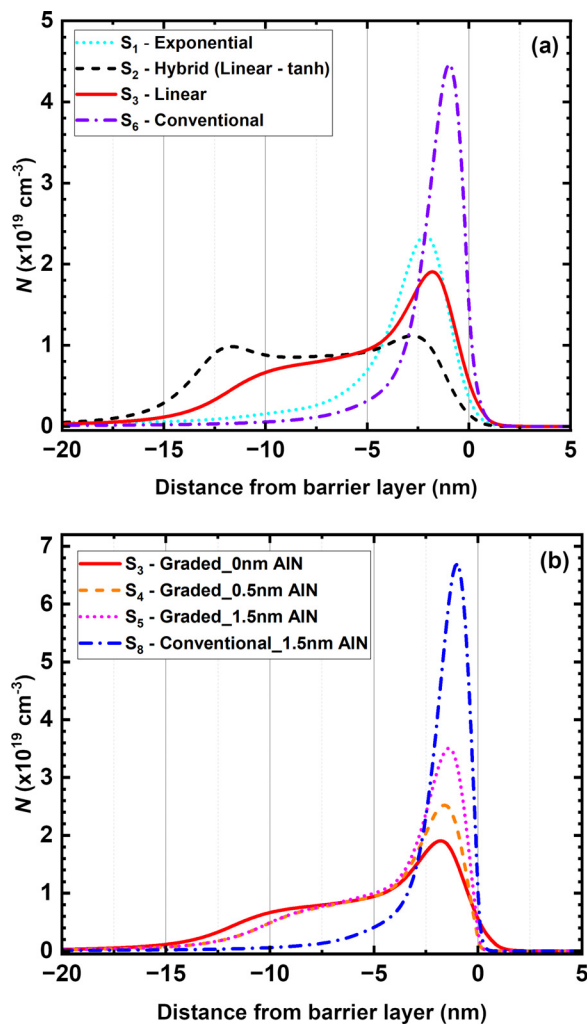


FIG. 3. Simulated electron density profiles for samples S_1 , S_2 , S_3 , and S_6 (a) and samples S_3 , S_4 , S_5 , and S_8 (b).

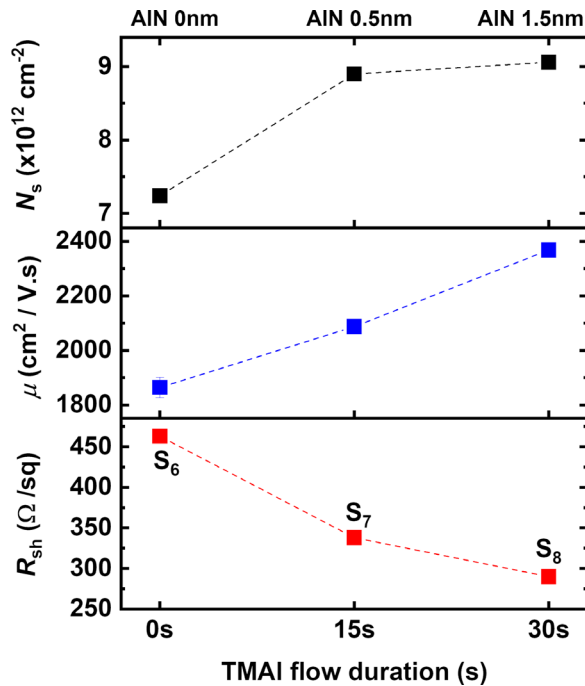


FIG. 4. 2DEG properties of conventional (non-graded channel) HEMT structures with different thicknesses of the AlN interlayer: 0 (S_6), 0.5 nm (S_7), and 1.5 nm (S_8) corresponding to TMAI flow duration of 0, 15, and 30 s. The dashed lines are guide for the eye.

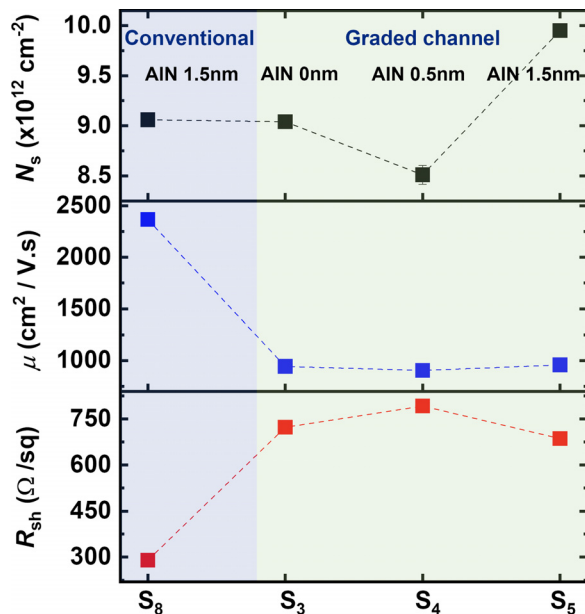


FIG. 5. 2DEG properties of the graded channel (S_3 , S_4 , and S_5) and conventional (S_8) HEMT structures. The AlN interlayer thickness is 0.5 nm for sample S_4 and 1.5 nm for samples S_5 and S_8 . Sample S_3 has no AlN interlayer. The dashed lines are guide for the eye.

its counterpart without AlN interlayer (S_3), indicating that the predominant effect on mobility is the alloy scattering in the Al-containing channel. However, the sheet resistance (R_{sh}) of S_5 is lower than that of S_3 , implying a partial improvement on the carrier confinement in the channel. This observation is also supported by the simulated electron density profiles in Fig. 3(b), where the 2DEG penetration in the barrier is minimized for S_5 compared to S_3 . Nonetheless, the improvement of the 2DEG properties as a result of incorporating an AlN interlayer is only marginal for the graded HEMT structures. The measured resistance of 686 Ω /sq for the graded channel (S_5) HEMT structure remains significantly higher than the respective value of 290 Ω /sq for the conventional counterpart S_8 .

In order to evaluate the direct current (DC) performance, HEMT devices were fabricated on the conventional non-graded and the linearly graded channel structures (S_8 and S_5). For the HEMTs fabrication, a “passivation-first” process scheme was applied with an *in situ* NH_3 pretreatment, to reduce surface native oxide and minimize surface-related trapping effects,²⁸ followed by a deposition of the 15 nm SiN passivation layer with low-pressure chemical vapor deposition. The device isolation was achieved through mesa etching. Recessed and Ta-based Ohmic contacts^{29,30} produced contact resistances of 0.30 – 0.35 Ω mm as extracted from transmission line measurements. The gate process includes two electron beam lithography (EBL) steps. The first step defines the etch mask for the recess in the SiN, which defines the gate length. The etching of the SiN passivation was performed by a combination of CF_4 + Ar plasma etching followed by NF_3 plasma etching. The second EBL step defines the pattern for the gate metallization (Au/Pt/Ni) with an integrated source and drain field plate of 0.1 and 0.25 μm , respectively. For HEMTs with gate lengths (L_g) of 100 and 200 nm, a gate-source distance (LGS) of 0.75 μm , gate-drain distances (LGD) of 1.5 μm , and a gate width of $2 \times 50 \mu\text{m}$ were fabricated. Figure 6 shows the DC transfer characteristics of the conventional non-graded channel (S_8 —blue) and the linearly graded channel (S_5 —magenta) HEMTs with $L_g = 0.2 \mu\text{m}$ (see Fig. S5 for results on $L_g = 0.1 \mu\text{m}$). Both devices have a threshold voltage (V_{th}) ~ -1.7 V. The maximum source-drain current density is 811 and 784 mA/mm, while the peak transconductance (g_m) at $V_{ds} = 4$ V is 369 and 308 mS/mm for the conventional and the graded channel HEMT, respectively. As shown in Fig. 6, the g_m is generally flat with smaller g'_m and g''_m for the HEMTs with graded channel. This is a measure of the expected linearity of the HEMTs as the third-order intermodulation distortion (IM3) is proportional to $(g''_m)^2$, and the third-order intercept point (IP3) is proportional to $(g_m)^3/g''_m$. It should be noted at this point that the measurements were performed on HEMTs with relatively long gate lengths and low V_{ds} in order to decrease short channel effects associated with the UID GaN buffer layer in these structures. Devices with Fe-doped buffer layers will be presented elsewhere.

In summary, we developed $\text{Al}_x\text{Ga}_{1-x}\text{N}$ graded channel HEMT structures with various graded profiles from $x = 0$ to $x = 0.1$ (exponential, hybrid tanh-linear, and linear) using hot-wall MOCVD. The Al-profiles, experimentally determined by EDS, were correlated with specific growth conditions, which can serve as guidelines for channel grading optimization in future works. It is shown that incorporating an AlN interlayer between the linearly graded channel and the barrier layer has only marginal effect on the 2DEG/3DEG properties in contrast to conventional $\text{AlGaIn}/\text{GaIn}$ HEMTs where significant improvement was observed. We find that although the mobility in

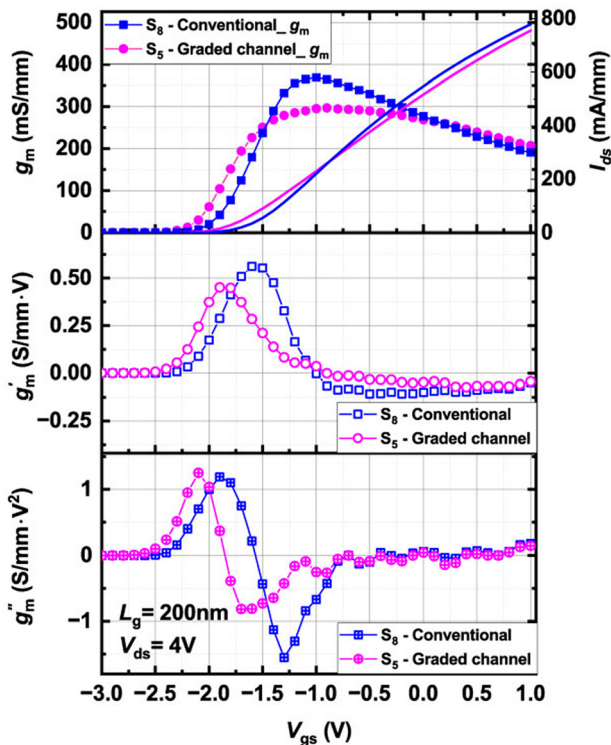


FIG. 6. DC transfer characteristics of the conventional non-graded channel (S_8 —blue) and the linearly graded channel (S_5 —magenta) HEMTs with $L_g = 0.2 \mu\text{m}$. The g_m , first derivative of g_m , and second derivative of g_m are plotted by filled, empty, and crossed symbols, respectively.

graded channel HEMT is limited by alloy scattering, the transconductance is generally flatter over a wider range of gate bias with smaller g'_m and g''_m as compared to conventional AlGaIn/GaN HEMTs. These features are required for highly linear devices used in low-noise RF amplifiers.

See the [supplementary material](#) for additional details about (i) the surface morphology (AFM images) of samples S_1 – S_3 , (ii) the VASE data analysis, (iii) the XRD reciprocal space maps of a conventional (S_7) and a graded channel (S_3) HEMT structure, (iv) the enlarged STEM image of the top region of S_3 (inset of Fig. 2), and (v) the DC transfer characteristics of the conventional non-graded channel (S_8) and the linearly graded channel (S_5) HEMTs with $L_g = 0.1 \mu\text{m}$.

This work was performed within the framework of the competence center for III-Nitride technology, C3NiT-Janzén supported by the Swedish Governmental Agency for Innovation Systems (VINNOVA) under the Competence Center Program Grant No. 2022-03139, Lund University, Linköping University, Chalmers University of Technology, Ericsson, Epiluvac, FMV, Gotmic, Hexagem, Hitachi Energy, On Semiconductor, Region Skåne SAAB, SweGaN, Volvo Cars and UMS. We further

acknowledge support from the Swedish Research Council VR under Award Nos. 2016-00889 and 2022-04812, Swedish Foundation for Strategic Research under Grant Nos. RIF14-055, EM16-0024 and STP19-0008 and the Swedish Government Strategic Research Area in Materials Science on Functional Materials at Linköping University, Faculty Grant SFO Mat LiU No. 2009-00971. The KAW Foundation is also acknowledged for the support of the Linköping Electron Microscopy Laboratory. P. O. Å. Persson acknowledges ARTEMI, the Swedish National Infrastructure in Advanced Electron Microscopy, through funding from the Swedish Research Council and the Foundation for Strategic Research (Grant Nos. 2021-00171 and RIF21-0026). The authors would like to thank Dr. Nerijus Armakavicius for general support on ellipsometry related discussions.

AUTHOR DECLARATIONS

Conflict of Interest

The authors have no conflicts to disclose.

Author Contributions

Alexis Papamichail: Conceptualization (equal); Data curation (lead); Formal analysis (lead); Investigation (lead); Visualization (equal); Writing – original draft (equal); Writing – review & editing (equal). **Plamen P. Paskov:** Investigation (equal); Writing – review & editing (equal). **Niklas Rorsman:** Conceptualization (equal); Formal analysis (equal); Investigation (equal); Resources (equal); Supervision (equal); Writing – review & editing (equal). **Vanya Darakchieva:** Conceptualization (equal); Funding acquisition (equal); Investigation (equal); Project administration (lead); Supervision (lead); Writing – review & editing (lead). **Axel R. Persson:** Formal analysis (equal); Investigation (equal); Writing – review & editing (equal). **Steffen Richter:** Formal analysis (equal); Investigation (equal); Writing – review & editing (equal). **Philipp Kühne:** Formal analysis (equal); Investigation (equal). **Vallery Stanishev:** Formal analysis (equal); Investigation (equal). **Per Persson:** Supervision (equal); Writing – review & editing (equal). **Ragnar Ferrand-Drake Del Castillo:** Investigation (equal). **Mattias Thorsell:** Conceptualization (equal); Methodology (equal); Writing – review & editing (equal). **Hans Hjelmgren:** Formal analysis (equal); Investigation (equal); Writing – review & editing (equal).

DATA AVAILABILITY

The data that support the findings of this study are available from the corresponding authors upon reasonable request.

REFERENCES

- ¹J.-S. Moon, J. Wong, B. Grabar, M. Antcliffe, P. Chen, E. Arkun, I. Khalaf, A. Corrion, J. Chappell, N. Venkatesan, and P. Fay, *IEEE Electron Device Lett.* **41**, 1173 (2020).
- ²S. Bajaj, Z. Yang, F. Akyol, P. S. Park, Y. Zhang, A. L. Price, S. Krishnamoorthy, D. J. Meyer, and S. Rajan, *IEEE Trans. Electron Devices* **64**, 3114 (2017).
- ³D. Jena, S. Heikman, D. Green, D. Buttari, R. Coffie, H. Xing, S. Keller, S. DenBaars, J. S. Speck, and U. K. Mishra, *Appl. Phys. Lett.* **81**, 4395 (2002).
- ⁴M. Ancona, J. Calame, D. Meyer, S. Rajan, and B. Downey, *IEEE Trans. Electron Devices* **66**, 2151 (2019).

- ⁵S. H. Sohel, A. Xie, E. Beam, H. Xue, T. Razzak, S. Bajaj, S. Campbell, D. White, K. Wills, Y. Cao, W. Lu, and S. Rajan, *Appl. Phys. Express* **13**, 036502 (2020).
- ⁶K. H. Hamza, D. Nirmal, A. A. Fletcher, L. Arivazhagan, J. Ajayan, and R. Natarajan, *AEU-Int. J. Electron. Commun.* **136**, 153774 (2021).
- ⁷B. Hou, L. Yang, M. Mi, M. Zhang, C. Yi, M. Wu, Q. Zhu, Y. Lu, J. Zhu, X. Zhou, L. Lv, X. Ma, and Y. Hao, *J. Phys. D* **53**, 145102 (2020).
- ⁸N. Venkatesan, G. Silva-Oelker, and P. Fay, in *IEEE BiCMOS and Compound Semiconductor Integrated Circuits and Technology Symposium (BCICTS)*, 2019.
- ⁹S. Rajan, S. P. DenBaars, U. K. Mishra, H. G. Xing, and D. Jena, *Appl. Phys. Lett.* **88**, 042103 (2006).
- ¹⁰J.-S. Moon, B. Grabar, J. Wong, D. Chuong, E. Arkun, D. V. Morales, P. Chen, C. Malek, D. Fanning, N. Venkatesan, and P. Fay, *IEEE Electron Device Lett.* **42**, 796 (2021).
- ¹¹J.-S. Moon, B. Grabar, J. Wong, C. Dao, E. Arkun, D. V. Morales, J. Tai, D. Fanning, N. Venkatesan, and P. Fay, in *IEEE Topical Conference on RF/Microwave Power Amplifiers for Radio and Wireless Applications (PAWR)* (IEEE, 2022), p. 5.
- ¹²S. H. Sohel, A. Xie, E. Beam, H. Xue, T. Razzak, S. Bajaj, Y. Cao, C. Lee, W. Lu, and S. Rajan, *IEEE Electron Device Lett.* **40**, 522 (2019).
- ¹³P. Fay, J.-S. Moon, and S. Rajan, *Appl. Phys. Lett.* **121**, 140502 (2022).
- ¹⁴F. Oehler, M. E. Vickers, M. J. Kappers, and R. A. Oliver, *J. Appl. Phys.* **114**, 053520 (2013).
- ¹⁵V. Darakchieva, B. Monemar, and A. Usui, *Appl. Phys. Lett.* **91**, 031911 (2007).
- ¹⁶W. Paszkowicz, S. Podsiadlo, and R. Minikayev, *J. Alloys Compd.* **382**, 100 (2004).
- ¹⁷T. Metzger, R. Höpler, E. Born, O. Ambacher, M. Stutzmann, R. Stömmer, M. Schuster, H. Göbel, S. Christiansen, M. Albrecht, and H. P. Strunk, *Philos. Mag. A* **77**, 1013 (1998).
- ¹⁸V. Srikant, J. S. Speck, and D. R. Clarke, *J. Appl. Phys.* **82**, 4286 (1997).
- ¹⁹P. Kühne, N. Armakavicius, V. Stanishev, C. M. Herzinger, M. Schubert, and V. Darakchieva, *IEEE Trans. Terahertz Sci. Technol.* **8**, 257 (2018).
- ²⁰S. Knight, S. Schöche, P. Kühne, T. Hofmann, V. Darakchieva, and M. Schubert, "Tunable cavity-enhanced terahertz frequency-domain optical hall effect," *Rev. Sci. Instrum.* **91**, 083903 (2020).
- ²¹M. Schubert, P. Kühne, V. Darakchieva, and T. Hofmann, *J. Opt. Soc. Am. A* **33**, 1553 (2016).
- ²²See <https://www3.nd.edu/~gsnider/> for "1D Poisson-Schrödinger solver."
- ²³I. Tan, G. L. Snider, L. D. Chang, and E. L. Hu, *J. Appl. Phys.* **68**, 4071 (1990).
- ²⁴J.-T. Chen, I. Persson, D. Nilsson, C.-W. Hsu, J. Palisaitis, U. Forsberg, P. O. Å. Persson, and E. Janzén, *Appl. Phys. Lett.* **106**, 251601 (2015).
- ²⁵M. E. Coltrin, A. G. Baca, and R. J. Kaplar, *ECS J. Solid State Sci. Technol.* **6**, S3114 (2017).
- ²⁶T. Huang, O. Axelsson, J. Bergsten, M. Thorsell, and N. Rorsman, *IEEE Electron Device Lett.* **38**, 926 (2017).
- ²⁷N. Armakavicius, J.-T. Chen, T. Hofmann, S. Knight, P. Kühne, D. Nilsson, U. Forsberg, E. Janzén, and V. Darakchieva, *Phys. Status Solidi C* **13**, 369 (2016).
- ²⁸D.-Y. Chen, A. R. Persson, K.-H. Wen, D. Sommer, J. Grünenpütt, H. Blanck, M. Thorsell, O. Kordina, V. Darakchieva, P. O. Å. Persson, J.-T. Chen, and N. Rorsman, *Semicond. Sci. Technol.* **37**, 035011 (2022).
- ²⁹A. Malmros, H. Blanck, and N. Rorsman, *Semicond. Sci. Technol.* **26**, 075006 (2011).
- ³⁰Y.-K. Lin, J. Bergsten, H. Leong, A. Malmros, J.-T. Chen, D.-Y. Chen, O. Kordina, H. Zirath, E. Y. Chang, and N. Rorsman, *Semicond. Sci. Technol.* **33**, 095019 (2018).